WPPFC-CPR(17) 16986

M Wirtz et al.

High pulse number thermal shock tests of tungsten with steady state particle background

Preprint of Paper to be submitted for publication in Proceeding of 16th International Conference on Plasma-Facing Materials and Components for Fusion Applications

This work has been carried out within the framework of the EUROfusion Consortium and has received funding from the Euratom research and training programme 2014-2018 under grant agreement No 633053. The views and opinions expressed herein do not necessarily reflect those of the European Commission.

High Pulse Number Thermal Shock Tests on Tungsten with Steady State Particle Background

M. Wirtz*, A. Kreter, J. Linke, Th. Loewenhoff, G. Pintsuk, G. Sergienko, I. Steudel, B. Unterberg, E. Wessel

Forschungszentrum Jülich, Institut für Energie- und Klimaforschung, 52425 Jülich, Germany

E-mail: m.wirtz@fz-juelich.de

Abstract. Experiments in the linear plasma device PSI-2 were used to investigate the synergistic effects of high pulse number thermal shock events (P = 0.38 GW/m^2, Δt = 0.5 ms) and stationary D/He (6 %) particle background on the thermo-mechanical fatigue behavior of tungsten. Similar to experiments with pure thermal loads, the induced microstructural and surface modifications such as recrystallization and roughening as well as crack formation become more pronounced with increasing number of thermal shock events. However, the amount of damage significantly increases for synergistic loads showing severe surface roughening, plastic deformation and erosion resulting from the degradation of the mechanical properties caused by bombardment and diffusion of H/He to the surface and the bulk of the material. Additionally, H/He induced blistering and bubble formation was observed for all tested samples, which changes the thermal and mechanical properties of near surface regions.

PACS: 28.52.Fa, 65.40.De, 62.20.me, 89.30.Jj

1. Introduction

The thermo-mechanical fatigue performance of metallic materials is one of the major concerns for any application, which exposes materials/components to repetitive high thermal loads. Since ITER will start with a full-tungsten (W) divertor, the thermal shock resistance of W became even more important due to the fact that high flux steady state plasma and transient edge localized modes (ELMs) striking could limit the lifetime of plasma facing materials (PFMs). During the service time of the divertor in ITER, millions of unmitigated type-I ELMs with energy densities up to 10 MJm^{-2} are expected to strike the divertor as well as a stationary heat flux of around 10 MWm^{-2} (for slow transients even up to

20 MWm^{-2}) [1,2]. The consequences of ELMs will be cracking, melting and erosion, which are potential impurity sources for the core plasma and have a strong influence on the lifetime of plasma facing components [3,4,5]. In addition, particle fluxes (H and He) will change the surface morphology by blistering and helium induced nanostructures, which affect the material properties and subsequently its performance [6,7]. Therefore, the synergistic effects of high pulse number transient heat loads in conjunction with stationary D/He (6 %) plasma were investigated in the linear plasma device PSI-2 [8] and compared with pure thermal exposure results obtained in former experiments in the electron beam device JUDITH 2 [9].

2. Material and experimental settings

An industrially produced tungsten forged bar material with a purity of 99.97 wt% provided by Plansee SE, Austria, was used for the experiments. Due to the production process the grain structure is strongly elongated [10]. Samples with the dimension 12 × 10 × 5 mm^3 were cut from the tungsten block with a transversal (grains elongated perpendicular to the loaded surface) and longitudinal (grains elongated parallel to the loaded surface) grain orientation. Additionally, some of the longitudinal samples were recrystallized in a vacuum furnace at 1600 °C for 1 h in order to investigate the influence of recrystallization and the associated change of the mechanical properties [11,12] on the thermal shock behavior. All samples were mechanically polished to a mirror finish to obtain an undamaged well-defined reference state.

The tests were executed in the linear plasma device PSI-2 at a base temperature of about 730 °C, which was achieved by the combination of the plasma exposure and an ohmic heater attached to the sample holder. A Nd:YAG laser with a wavelength of 1064 nm, a maximum energy of 32 J and a beam diameter of ~3 mm was used to simulate the ELM-like transient thermal events. 10^4 and 10^5 of such thermal shock events were applied on the sample surface. The used parameters were an absorbed power density of 0.38 GW/m^2, which is above the damage threshold of this material [10] and results in a temperature increase in the range of 700 – 800 °C (based on FEM simulations), a pulse duration of 0.5 ms, and a repetition frequency of 10 Hz. The variation of the base temperature during the thermal

shock exposure was in the range of 15 – 20 °C and is therefore negligible. The steady state exposure was realized by mixed D/He (6 %) plasma with a particle energy of ~35 eV and a flux of about 6×10^{21} $m^{-2}s^{-1}$. This corresponds to a fluence of 9×10^{24} m^{-2} (10^4 pulses) and 6×10^{25} m^{-2} (10^5 pulses), respectively.

After the exposure in PSI-2, the induced damages and surface modifications were analyzed by metallographic means (cross sections), light microscopy (LM), scanning electron microscopy (SEM), electron backscatter diffraction (EBSD) and focused ion beam (FIB) cross sections.

3. Results and discussion

All investigated samples were simultaneously exposed to ELM-like heat loads and a stationary particle background as explained in section 2. SEM images of the induced surface modifications and damages of the transversal samples, which are representative for all three tested grain orientations, are shown in Figure 1.

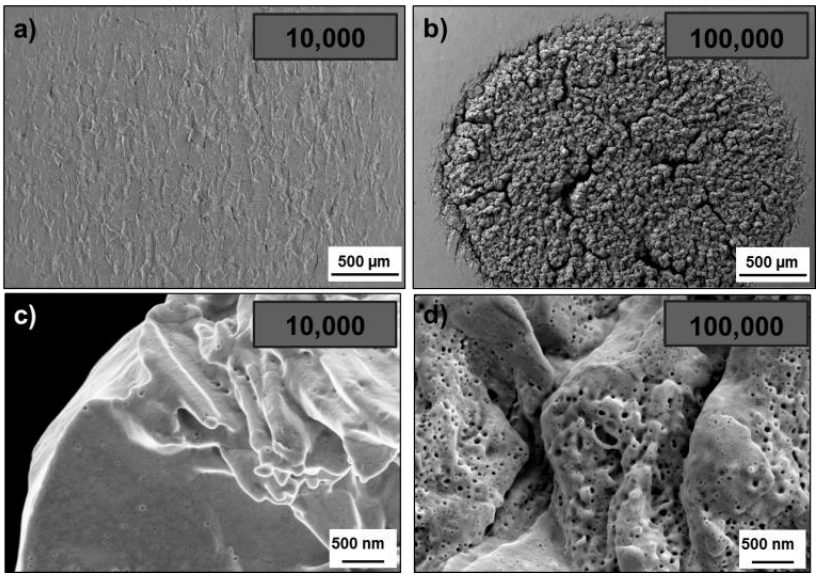

Figure 1: SEM images of the samples with transversal grain orientation simultaneously exposed to thermal shocks of 0.38 GW/m² and stationary particle background: (a) and (c) after the exposure to 10^4 thermal shocks; (b) and (d) after the exposure to 10^5 thermal shock events.

The accumulation of damage for increasing number of thermal shock pulses is clearly visible by comparing Figure 1a and b. After 10^4 pulses only slight roughening due to plastic deformation is observed and some isolated small arbitrarily distributed cracks are visible within the laser exposed area. In contrast to that, the loaded surface appears severely deformed after 10^5 pulses. The roughening

increases significantly and the cracks become much larger and form a network. Some cracks even propagate in the only plasma exposed surrounding material. At a higher magnification (Figure 1c and d) a porous structure becomes visible, which is much more pronounced after 10^5 pulses. These structures could originate from small He filled bubbles that form below the surface and become visible due to erosion during exposure. These structures are also visible in the only plasma exposed surrounding material. This accumulation of surface damages with increasing number of thermal shock events was observed for all three investigated grain structures.

Laser profilometry measurements of the arithmetic mean roughness (R_a) depicted in Table 1 confirm the increase of the surface roughness due to plastic deformation with increasing number of thermal shock events. This increase is very pronounced for the transversal (T) and longitudinal (L) grain orientation. In contrast, the recrystallized (R) samples exhibit the highest roughness values after 10^4 pulses while there is only a slight increase observed when proceeding to 10^5 pulses, resulting in the by far lowest roughness values among all tested microstructural options. This difference in the accumulation of plastic deformation can be traced back to the differences in the mechanical properties of the three grain structures. Tensile tests performed at 1000 °C exhibit high strength/low ductility of the transversal and longitudinal grain orientation (T: fracture strain ≈ 22 %, yield strength (0.2%) ≈ 370 MPa; L: fracture strain ≈ 17 %, yield strength (0.2%) ≈ 340 MPa) and lower strength/higher ductility of the recrystallized material (fracture strain ≈ 68 %, yield strength (0.2%) ≈ 100 MPa) [13]. The significant drop of the mechanical strength results in a faster damage evolution during the first 10^4 pulses compared with the T and L orientation but, associated with an increase of the fracture strain after recrystallization caused by the reduction of the production related induced stresses and defects (mainly dislocations) [14,15], a slower increase at higher pulse numbers.

Table 1: Overview of the arithmetic mean roughness (R_a) values in µm of all tested samples/grain structures.

grain structure	**T**	**L**	**R**
10,000 pulses	1	2	4
100,000 pulses	22	36	6

The damage evolution/accumulation during the thermal shock exposure is also reflected in the metallographic cross sections of the exposed samples. Figure 2 shows LM images of the cross sections prepared from the transversal samples after 10^4 (Figure 2a) and 10^5 (Figure 2b) pulses. After 10^4

thermal shock events some small cracks, similar to Figure 1a/c, are visible. Additionally, indications for changes of the microstructure such as sub-grain formation, grain nucleation and recrystallization can be found in a very shallow surface region. However, this changes drastically after the exposure to 10^5 pulses. The microstructural changes become more pronounced and distinct hill/valley structures are formed (Figure 2b), which can be observed for all three tested grain orientations. Table 2 gives an overview about the magnitude of the hill/valley structures, which was measured from the pristine surface and is exemplarily indicated by the dashed line in Figure 2b. The differences in height, which reach on some samples more than 400 µm, are an indication for erosion of larges parts of the loaded surface, leading to dust formation and in the worst-case contamination of the core plasma. Furthermore, these structures are prone to overheating and melting, especially, if you take a low incident angle of the particles into account, as it will be the case in a device like ITER.

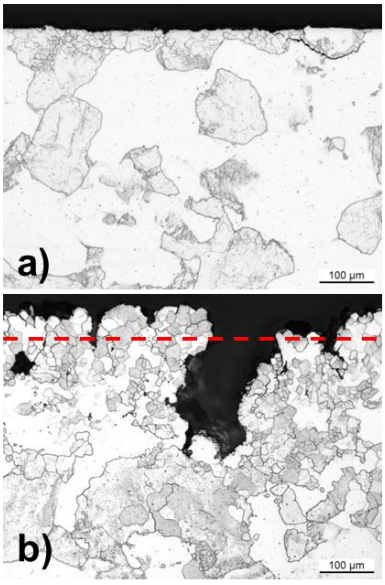

Figure 2: LM images of the cross section prepared from the transversal samples exposed to (a) 10^4 and (b) 10^5 thermal shock events with a power density of 0.38 GW/m² and with simultaneous plasma background. The dashed line indicates in (b) the level of the pristine surface before the exposure.

Table 2: Maximum magnitude in µm of the hill and valley structures after the exposure to 10^5 thermal shock events measured from the pristine surface before the exposure.

grain structure	T	L	R
hills	87	145	53
valleys	-193	-280	-24

In order to investigate the additional influence of the simultaneous particle exposure during the thermal shock loading on the long term damage behavior of tungsten, the obtained results from the PSI-2 experiments were compared with pure thermal experiments conducted with the same material in

the electron beam device JUDITH 2 [4,9]. SEM/LM images of the induced surface modifications/damages of the transversal samples after the exposure to 10^5 thermal shock events in PSI-2 and JUDITH 2 are shown in Figure 3. Thermal shock crack networks were induced on both surfaces. However, the sample with simultaneous plasma exposure (Figure 3a) show a much stronger deformation of the surface than the pure thermal exposed one (Figure 3b). This is confirmed by the measured R_a (Table 3) values, which are more than twice as high with additional particle background. The metallographic cross sections (Table 3c and d) reveal that the synergistic loads cause a much faster accumulation of damage resulting in an increased risk of material loss compared to the pure thermal exposure. These results can be traced back to D/He embrittlement and the associated degradation of the mechanical properties/strength of the material [14]. Furthermore, after the pure thermal exposure the recrystallized material shows the lowest surface roughness compared to the T and L samples, which was also observed after the laser + plasma exposure and can be related to the higher ductility compare to the other two grain orientations.

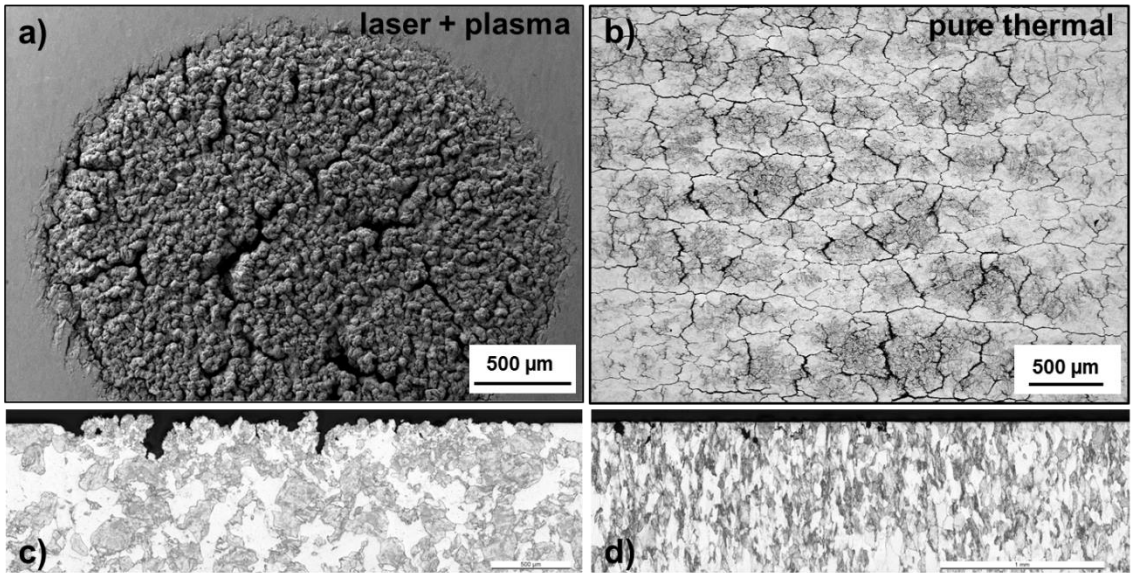

Figure 3: SEM images of the loaded surface (transversal sample) and LM of the corresponding cross sections after the exposure to 10^5 thermal shock events in PSI-2 (a + c) with additional particle background and in JUDITH 2 (b + c), which was a pure thermal exposure.

Table 3: Overview of the arithmetic mean roughness (R_a) values in µm of all tested samples/grain structures after the exposure to 10^5 thermal shock events.

grain structure	T	L	R
laser + plasma (PSI-2)	22	36	6
pure thermal (JUDITH 2)	2	15	3

EBSD band contrast images (Figure 4) were taken in order to investigate microstructural changes that were already observed in the LM images of the cross sections (Figure 2). Already after 10^4 thermal shock evets microstructural changes become visible in some parts of the surface with a depth of around 90 µm. This region increases with the number of pulses to a depth of around 300 µm after 10^5 thermal shock events. These microstructural changes comprise the formation of sub-grains, grain nucleation, and grain refinement due to recrystallization/dynamic recrystallization and were observed for all three investigated microstructures, including the samples that were recrystallized before the exposure at 1600 °C for 1 h. The depth of this region after 10^5 thermal shock events was nearly the same for all types of exposed samples and is in good agreement with the depth of the thermal gradients induced during the thermal shocks. This leads to the assumption, that there might be thermal penetration related saturation at higher number of pulses, which requires further experiments with higher pulse numbers. Nevertheless, these microstructural changes have an impact on the mechanical properties of the material and maybe also the diffusion/retention of D/He as it was reported for lower pulse number tests in [15].

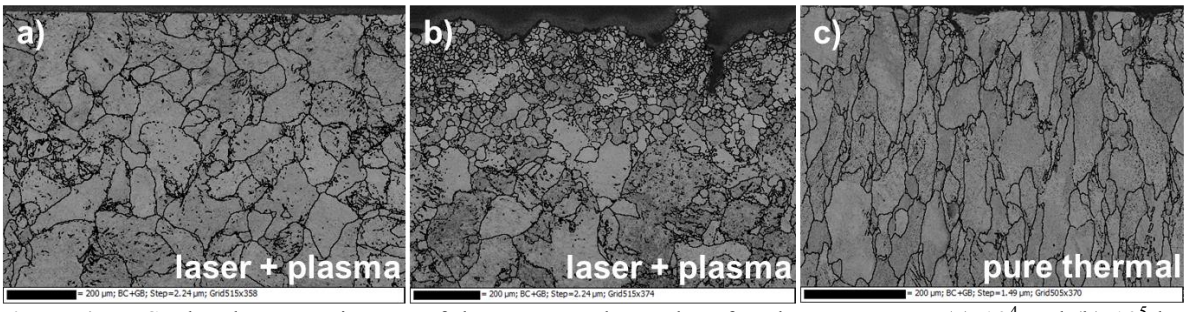

Figure 4: EBSD band contrast images of the transversal samples after the exposure to (a) 10^4 and (b) 10^5 laser pulses in PSI-2. (c) shows the transversal sample exposed in JUDITH 2 after 10^5 thermal shock events without particle background. The black lines indicate grain boundaries with an angle mismatch ≥ 5°.

The comparison of the EBSD images after the laser + plasma (Figure 4b) and pure thermal (Figure 4c) exposure shows again a clear difference between the two exposure methods. In contrast to the samples exposed in PSI-2, the pure thermally loaded samples show no or only slight changes of the microstructure. Based on earlier studies [16] it can be assumed that this difference is not caused by using a laser or electron beam to simulate the thermal shocks but by the additional stationary D/He particle background during the PSI-2 exposure. Results presented in [17,18] exhibit that the exposure of tungsten to a stationary D plasma leads to an increased defect/dislocation density as well as a

change of the mechanical properties (increase of hardness). In combination with the additional thermal shock exposure in PSI-2, which induces high thermal gradient and stresses in the near surface region, this first indications to explain the observed difference in the microstructure of tungsten after the exposure in PSI-2 and JUDITH 2. However, additional experiments and investigations are required to understand the underlying effects and interactions in more detail.

SEM images of FIB cuts at representative positions of the laser + plasma and the only plasma exposed surrounding sample surface, shown in Figure 5, reveal He induced bubble formation below the exposed surface. After 10^4 thermal shock events (fluence ~9×10^{24} m^{-2}) no visible He bubble formation was observed below the only plasma exposed surface, while below the laser + plasma exposed surface He bubbles were found (Figure 5a). The depth of the He effected layer and the average diameter of the bubbles are given in Table 4 for all three microstructures.

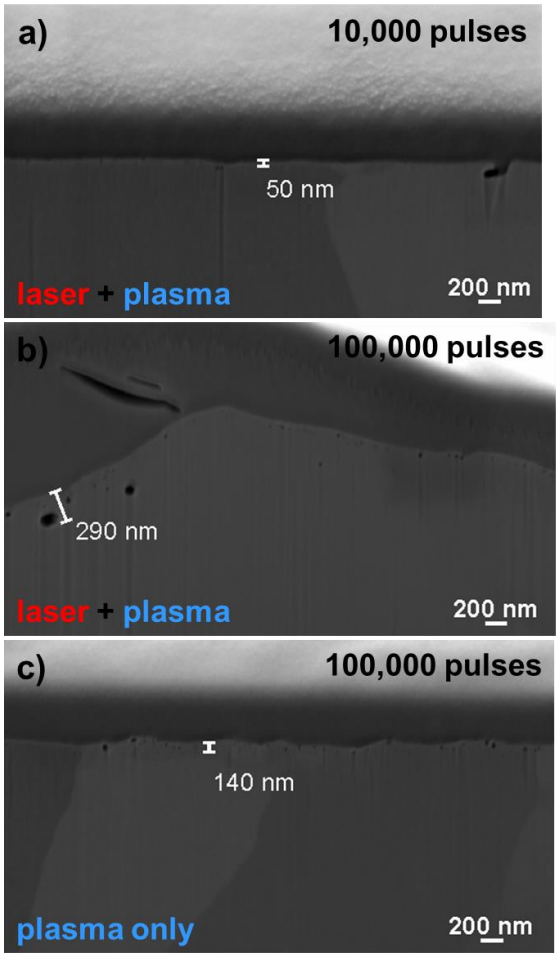

Figure 5: SEM images of the FIB cuts performed on the transversal samples after the exposure in PSI-2: (a) below the laser + plasma exposed spot after 10^4 pulses; (b) below the laser + plasma exposed spot after 10^5 pulses; (c) only plasma exposed surface outside the laser spot after 10^5 pulses.

Table 4: Size of the He effected layer and the average diameter of the He bubbles after 10^4 laser pulses. All values are in nm.

grain structure	T	L	R
size of layer	50	140	140
average diameter	30	75	16

For 10^5 thermal shock events and a fluence of ~6×10^{25} m^{-2} He bubbles were observed below the laser + plasma as well as below the only plasma exposed surface (Figure 5b + c) which can be explained by the higher fluence. A direct comparison of the size of the He effected layer and the average bubble diameter shows that both values increase with increasing number of pulses/fluence. The additional transient heat loads lead to a further extension of the He affected layer as well as a larger size of the He bubbles. Higher thermal gradients/surface temperatures induced by the thermal shocks could cause accelerated/deeper diffusion of He into the bulk material. This results in these differences between the laser + plasma and the only plasma exposed surface.

Table 5: Size of the He effected layer and the average diameter of the He bubbles outside (plasma only) and below the laser spot after 10^5 pulses. All values are in nm.

grain structure	T	L	R
size of layer (outside)	140	210	100
size of layer (below)	290	240	400
average diameter (outside)	36	60	23
average diameter (below)	103	75	56

The increase of the He affected layer as well as of the size of the He bubbles may also result in a larger and more distinct zone with altered thermal and mechanical properties such as hardening and reduction of the thermal conductivity [19], having a direct impact on the thermal shock performance of the material [4,12]. Furthermore, these damages beneath the surface will change/impact the retention behavior of tungsten [19].

4. Summary & Conclusion

Tungsten samples with different microstructures were simultaneously exposed to 10^4 and 10^5 ELM like transient thermal loads in combination with a stationary H/He plasma background in the linear plasma device PSI-2 to investigate the impact of synergistic loads on the long term damage behavior of tungsten. The obtained results show an accumulation of plastic deformation for increasing number of thermal shock events due to the repetitive induced compressive/tensile thermal stresses [12]. This is

a clear indication for thermal fatigue effects. Beside the plastic deformation also cracks/crack networks and pronounced hill/valley structures are formed on the exposed surfaces. These surface structures give evidence of enhanced erosion and loss of large parts of the surface material what could lead to local over heating/melting and contamination of the core plasma. Furthermore, the damage evolution of recrystallized material seem to start much faster than for the transversal and longitudinal grain structures but show some kind of saturation or at least slower damage evolution after 10^5 thermal shock events. This could be related to the higher fracture strain/ductility of the material. Additionally, microstructural changes like grain nucleation, subgrain formation and dynamic recrystallization were observed for all three grain structures, which will change the mechanical properties during the exposure.

A comparison of the induced surface modification and damages after the simultaneous thermal shock and particle exposure with pure thermal exposure results performed in the electron beam facility JUDITH 2 exhibit that the additional stationary particle background changes the thermal shock damage response of tungsten significantly. The damage evolution is much faster, the induced damages are more severe (e.g. hill/valley structures) and the microstructural changes are more pronounced with additional D/He particle background.

A growth of the He induced nano-bubbles as well of the He effected layer due to the rapid heating during the transient thermal events was observed. Further studies are needed to clarify if this affects the D/He retention and also increases the zone of increased hardness/reduced thermal conductivity.

Based on these results and the comparison with the pure thermal exposure of the same tungsten material it can be stated that stationary particle background has a significant influence on the long term damage performance of tungsten as PFM. Changes of the mechanical, thermal and microstructural properties seem to be induced or at least accelerated due to H/He embrittlement. Because of the strong correlation between material properties and the damage behavior/life time of PFMs, these additional degradations/changes could cause severe problems like enhanced erosion, cracking, overheating/melting and plasma contamination for the long term operation of future fusion devices. However, further experiments to quantify the material erosion and the degradation of the material

properties are needed. Another important issue for future experiments is the impact of n irradiation on the life time of PFM/PFC, which has not been taken into account yet.

Acknowledgements

This work has been carried out within the framework of the EUROfusion Consortium and has received funding from the Euratom research and training programme 2014-2018 under grant agreement No 633053. The views and opinions expressed herein do not necessarily reflect those of the European Commission. This work was done within the EUROfusion work program PFC.

References

[1] R.A. Pitts, S. Carpentier, F. Escourbiac, T. Hirai, V. Komarov, S. Lisgo, A.S. Kukushkin, A. Loarte, M. Merola, A. Sashala Naik, R. Mitteau, M. Sugihara, B. Bazylev, P.C. Stangeby. Journal of Nuclear Materials 438 (2013) S48-S56

[2] A. Loarte, G. Saibene, R. Sartori, V. Riccardo, P. Andrew, J. Paley, W. Fundamenski, T. Eich, A. Herrmann, G. Pautasso, A. Kirk, G. Counsell, G. Federici, G. Strohmayer, D. Whyte, A. Leonard, R. A. Pitts, I. Landman, B. Bazylev, S. Pestchanyi. Physica Scripta, (2007) 222-228

[3] Pintsuk G, Prokhodtseva A and Uytdenhouwen I 2011 Thermal shock characterization of tungsten deformed in two orthogonal directions *Journal of Nuclear Materials* **417** 481-486

[4] M. Wirtz, J. Linke, Th. Loewenhoff, G. Pintsuk, I. Uytdenhouwen; Transient Heat Load Challenges for Plasma-Facing Materials during Long-Term Operation; Nuclear Materials & Energy (2016) (in Press).

[5] Philipps V 2011 Tungsten as material for plasma-facing components in fusion devices *Journal of Nuclear Materials* **415** S2-S9

[6] G. de Temmerman, T. Morgan et al.; Effect of high-flux H/He plasma exposure on tungsten damage due to transient heat loads; Journal of Nuclear Materials 463 198 – 201 (2015)

[7] H. Xu, G. Luo et al.; Enhanced modification of tungsten surface by nanostructure formation during high flux deuterium plasma exposure; Journal of Nuclear Materials 447 (1–3) 22 – 27 (2014)

[8] A. Kreter, et al., Fusion Science and Technology 68 8 – 14 (2015)

[9] Th. Loewenhoff et al., Fusion Engineering and Design 87 (2012), 1201-1205

[10] G. Pintsuk et al., Journal of Nuclear Materials 417 (1 – 3) 481 – 486 (2011)

[11] F. J. Humphreys, M. Hatherly, Recrystallization and Related Annealing Phenomena, Pergamon 2nd edition (2003)

[12] M. Wirtz, I. Uytdenhouwen, V. Barabash, F. Escourbiac, T. Hirai, J. Linke, Th. Loewenhoff, S. Panayotis, G. Pintsuk; Material Properties and Their Influence on the Behaviour of Tungsten as Plasma Facing Material; Nuclear Fusion 57 (6) 066018 (2017).

[13] I. Uytdenhouwen; Degradation of First Wall Materials under ITER Relevant Loading Conditions; Ph.D. thesis Universiteit Gent (2010).

[14] R.P. Jewett, R.J. Walter, W.T. Chandler, and R.P. Frohmberg. Hydrogen Environment Embrittlement of Metals. NASA CR-2163, 1973.

[15] A. Huber et al. Physica Scripta T167, art. no. 014046 (2016)

[16] M. Wirtz et al. Journal of Nuclear Materials 438, S833-S836 (2013).

[17] A. Dubinko et al. Nuclear Instruments and Methods in Physics Research B 393 (2017) 155–159.

[18] A. Dubinko et al. Applied Surface Science 393 (2017) 330–339.

[19] N. Yoshida, H. Iwakiri, K. Tokunaga, T. Baba. Journal of Nuclear Materials 337-339 (2005) 946-950.